Received: 26 August 2024 | Revised: 15 October 2024 | Accepted: 23 October 2024

DOI: 10.1111/jace.20251

Journal of the American Ceramic Society

RESEARCH ARTICLE

CMAS corrosion resistance of rare earth phosphates at high temperatures for environmental barrier coatings

Bishnu Pada Majee[1,2] | **Keith Bryce**[2] | **Liping Huang**[1] | **Jie Lian**[1,2]

[1]Department of Materials Science and Engineering, Rensselaer Polytechnic Institute, Troy, New York, USA

[2]Department of Mechanical, Aerospace and Nuclear Engineering, Rensselaer Polytechnic Institute, Troy, New York, USA

Correspondence
Jie Lian, Department of Materials Science and Engineering, Rensselaer Polytechnic Institute, Troy, NY 12180, USA.
Email: lianj@rpi.edu

Funding information
National Science Foundation, Grant/Award Number: DMREF-2119423

Abstract

Phase stability, thermal properties, and calcium–magnesium–alumina–silicate (CMAS) resistance of $LuPO_4$ at 1300°C, 1400°C, and 1500°C were studied to evaluate its potential as an environmental barrier coating (EBC) for SiC-based ceramic-matrix composites (CMCs). Its coefficient of thermal expansion ($\sim 5.69 \times 10^{-6}\,°C^{-1}$) is close to that of SiC-based CMCs. At 1300°C, a dense reaction layer of $Ca_8MgLu(PO_4)_7$ forms and inhibits CMAS penetration; however, no such layer forms at 1400°C and 1500°C, leading to CMAS infiltration along grain boundaries. Prolonged (45 and 96 hours) CMAS corrosion of $LuPO_4$ at 1300°C showed the formation of a disilicate ($Lu_2Si_2O_7$) phase along with $Ca_8MgLu(PO_4)_7$. A multicomponent rare earth phosphate $(Lu_{0.2}Yb_{0.2}Er_{0.2}Y_{0.2}Gd_{0.2})PO_4$ shows improved CMAS resistance at 1400°C due to higher grain boundary stability and slower dissolution rate of rare earth elements into molten CMAS than single component rare earth phosphate. The mechanisms of CMAS corrosion and the kinetics of the formation of protective reaction layers in $LuPO_4$ and $(Lu_{0.2}Yb_{0.2}Er_{0.2}Y_{0.2}Gd_{0.2})PO_4$ were elucidated. Multicomponent design is needed to increase grain boundary stability and reduce dissolution rate into molten CMAS for $REPO_4$-based EBCs.

KEYWORDS

calcium–magnesium–alumina–silicate (CMAS) corrosion, environmental barrier coatings (EBCs), $LuPO_4$, multicomponent $REPO_4$, thermal properties

1 | INTRODUCTION

The increasing demand for more powerful, higher fuel-efficient, and environment-friendly gas turbine engines for aerospace and energy generation applications requires the development of new materials/technologies.[1–3] Ni-based superalloys have been used in the gas turbine engine's hot section, and under a harsh environment, water vapor, a byproduct of fuel combustion, along with residual oxygen from the combustion process, readily oxidize the engine's components under operation conditions.[4,5] Due to an increase in the operating temperature of gas turbine engines, Ni-based superalloys are incompatible because their melting temperature is close to the engine's operating temperature. SiC/SiC ceramic matrix composites (CMCs) are the most promising material to fill this gap due to their outstanding properties, such as exceptional mechanical properties, low density, and high-temperature performance.[6,7] CMCs provide an increased operating temperature and higher strength than Ni-based superalloys at high temperatures.[8] They show good oxidation and corrosion resistance at high temperatures under clean and dry oxygen environments due to the formation of a protective SiO_2 layer. However, in the presence of

calcium–magnesium–alumina–silicate (CMAS) and water vapor at high temperatures, CMCs degrade slowly.[9,10] To protect the surface of CMCs at high temperatures, environmental barrier coatings (EBCs) were introduced[11–14] in order to extend their service life. EBC candidates typically require high-temperature stability, matched coefficients of thermal expansion (CTEs) with CMCs, low thermal conductivity, and high CMAS and water vapor corrosion resistance.[3,15,16]

Potential candidates for the EBC application are rare earth elements-containing materials due to their excellent properties. The current generation EBCs are rare earth silicates (mono- or disilicates) such as lutetium and ytterbium silicates.[17–20] Di-silicate materials such as $Lu_2Si_2O_7$ (CTE ~3.8 × 10^{-6} K^{-1} in temperature range 473–1773 K) and $Yb_2Si_2O_7$ (CTE ~4.1. × 10^{-6} K^{-1} in temperature range 293–1723 K) have CTEs that closely match with that of the SiC–CMC substrate, but monosilicates such as Lu_2SiO_5 (CTE ~7.2 × 10^{-6} K^{-1} in temperature range 473–1623 K) and Yb_2SiO_5 (CTE ~7.2 × 10^{-6} K^{-1} in temperature range 473–1623 K) have higher CTEs.[21,22] A study by Nasiri et al. highlighted that rare earth mono-silicates RE_2SiO_5 (RE = Y, Yb, Er, and Lu) had great potential for the topcoat of EBCs after studying their thermal properties such as CTE and thermal conductivity.[22] The main drawback is that mono- or disilicate EBCs suffer from water vapor corrosion at 1200°C due to the volatility of the reaction product silica at high temperatures.[8] CMAS corrosion is another hurdle for rare earth silicates as EBCs. During the landing and takeoff, CMAS occurs when engines ingest environmental debris such as volcanic ash, sand, and dust.[19] CMAS reacts with rare earth silicates at high temperatures, forming unfavorable new crystalline phases with high CTEs and low stability that are undesirable for EBC applications.[2,23–25]

Recently, rare-earth phosphates ($REPO_4$) have been explored as new EBCs as they show suitable properties, such as high melting temperature, low thermal conductivity, matched CTEs close to SiC-CMCs, high-temperature phase stability and good CMAS and water vapor resistance at high temperatures.[26–29] Han et al. investigated the mechanical and thermophysical properties of xenotime rare earth phosphates $REPO_4$ (RE = Lu, Yb, Er, Y, and Sc),[26] and proposed that these materials are suitable for the topcoat of EBC materials. Wang et al. investigated the high-temperature thermomechanical properties and water vapor corrosion of yttrium phosphate (YPO_4), which displays a similar CTE to SiC–CMCs, and good water vapor resistance at 1350°C due to the absence of Si-O bonds.[30] Hu et al. investigated the interaction of $LuPO_4$ with CMAS at 1300°C and found that a dense and continuous reaction layer formed at the CMAS/$LuPO_4$ interface.[15] Recently, Ridley et al. investigated the thermomechanical properties and thermochemical stability of $YbPO_4$. They also carried out CMAS tests at 1300°C for 4, 24, and 96 hours and observed the formation of a reaction layer at the CMAS/$YbPO_4$ interface.[31] None of the above studies tested CMAS corrosion of $REPO_4$ at high temperatures (1400°C and 1500°C).

With the gas inlet temperature of gas turbine engine increasing up to 1773 K,[5,32] the next-generation EBC materials need good stability and CMAS corrosion resistance at higher temperatures.[32] In the past decade, the CMAS corrosion resistance of mono- and disilicate materials at high temperatures (1400°C and 1500°C) have been investigated.[19,20,33–35] For example, Zhao et al. comprehensively investigated the CMAS corrosion behavior of ytterbium monosilicates (Yb_2SiO_5) at 1400°C and 1500°C for different durations (5, 25, and 50 hours).[20] Their study showed that at 1400°C, a continuous reaction layer $Ca_2Yb_8(SiO_4)_6O_2$ tended to form at the CMAS/Yb_2SiO_5 interface, which effectively inhibited molten CMAS penetration into Yb_2SiO_5. However, at 1500°C, a dense and continuous layer could hardly form, limiting the protective capabilities of Yb_2SiO_5. Wiesner et al. studied CMAS corrosion of yttrium disilicate ($Y_2Si_2O_7$) at 1200°C, 1300°C, 1400°C, and 1500°C for 20 hours in air. They found that oxyapatite silicate $Ca_2Y_8(SiO_4)_6O_2$ phase formed by the dissolution of $Y_2Si_2O_7$ into molten CMAS and reaction with CaO at all temperatures, but $Y_2Si_2O_7$ does not appear to adequately arrest CMAS attack through the formation of a reaction layer at 1400°C and 1500°C for 20 h.[24] Sun et al. studied high-temperature CMAS resistance of a multicomponent β-$(Er_{0.25}Tm_{0.25}Yb_{0.25}Lu_{0.25})_2Si_2O_7$ disilicate at 1400°C and 1500°C and showed enhanced CMAS corrosion resistance as compared with single component disilicates (γ-$Y_2Si_2O_7$, β-$Yb_2Si_2O_7$, and β-$Lu_2Si_2O_7$).[35] Recently, Bryce et al. studied the CMAS (40CaO–5MgO–5$AlO_{1.5}$–50SiO_2) corrosion resistance of a high entropy rare earth phosphate ($Lu_{0.2}Yb_{0.2}Er_{0.2}Y_{0.2}Gd_{0.2}$)$PO_4$ at 1300°C–1500°C.[11] They observed the formation of a reaction layer at 1300°C and 1400°C, which halts the CMAS penetration up to certain limits. At 1400°C, the reaction layer was not homogenous, and its thickness was 20 to 90 μm. However, at 1500°C, CMAS penetrates into the bulk pellet via grain boundaries.[11] CMAS corrosion resistance at high temperatures of 1400 or 1500°C is essential for the performance of silicate and phosphate materials as potential EBCs. To the best of our knowledge, there are no reports on the CMAS corrosion of single-component xenotime rare earth phosphate at temperatures higher than 1300°C. Hence, the corrosion mechanism and reaction product against molten CMAS corrosion at higher temperatures (i.e., 1400 and 1500°C) remain unclear. In this work, we carried out CMAS (33CaO-9MgO-13$AlO_{1.5}$-45SiO_2) corrosion tests at 1300–1500°C for various

durations to understand the reaction mechanism and the interfacial layer formation in $LuPO_4$ in order to evaluate its corrosion resistance at higher temperatures and explore its potential as a new EBC. The CMAS corrosion of $(Lu_{0.2}Yb_{0.2}Er_{0.2}Y_{0.2}Gd_{0.2})PO_4$ was also tested at 1400°C for 5 hours to compare its performance with single-component $LuPO_4$.

In this work, $LuPO_4$ powders were synthesized via the chemical co-precipitation and calcination process and consolidated into dense pellets by spark plasma sintering (SPS). Its structure, thermal stability, CTE, and thermal conductivity were characterized. The CMAS resistance of the SPS-densified $LuPO_4$ sample was investigated at 1300°C for 5, 45, and 96 hours, at 1400°C for 5 hours, and at 1500°C for 1 and 5 hours. For a direct comparison, CMAS resistance of $(Lu_{0.2}Yb_{0.2}Er_{0.2}Y_{0.2}Gd_{0.2})PO_4$ was performed at 1400°C for 5 hours using the same CMAS ($33CaO–9MgO–13AlO_{1.5}–45SiO_2$) composition as for $LuPO_4$. Post-corrosion characterizations were carried out to analyze the reaction products, the interfacial layer growth rate, and mechanisms. The primary objective of this study is to understand the CMAS corrosion at high temperatures in single and multicomponent rare earth phosphate and leverage this knowledge to improve the design of $REPO_4$ as an EBC material at high temperatures.

2 | MATERIALS AND METHODS

2.1 | Material preparation

Xenotime-type $LuPO_4$ was prepared by chemical coprecipitation and annealing techniques. Lu_2O_3 (99.99%, Alfa Aesar), 70 wt% HNO_3 and 85 wt% H_3PO_4 were used as initial feedstock materials. Two chemical reactions took place during the synthesis, as follows.

$$Lu_2O_3\,(s) + 6\,HNO_3\,(1) \rightarrow 2\,Lu(NO_3)_3(aq) + 3\,H_2O\,(1) \quad (1)$$

$$Lu(NO_3)_3\,(aq) + H_3PO_4\,(l) \rightarrow LuPO_4\,(aq) + 3HNO_3\,(l) \quad (2)$$

Lu_2O_3 powders were added to the DI water with excess HNO_3 mixture solution, and the solvent mixture was stirred at 400°C for 5 hours to obtain $Lu(NO_3)_3$, followed by the addition of H_3PO_4 to reduce $Lu(NO_3)_3$ to $LuPO_4$ ultimately. White precipitate $LuPO_4$ powders were filtered and washed in DI water several times and dried overnight at 90°C in a box furnace. The prepared $LuPO_4$ powders were calcined at 1000°C for 12 hours and ground via an agate mortar and pestle into fine powders for sintering.[11] The details of the synthesis of $(Lu_{0.2}Yb_{0.2}Er_{0.2}Y_{0.2}Gd_{0.2})PO_4$ can be found in our previously published article.[11]

2.2 | $LuPO_4$ sintering

$LuPO_4$ pellets were sintered in an Ar environment using a SPS (Model 10 - 3 SPS system, Thermal Tech. LLC). 1 gram of calcined powders were put in a 10 mm diameter graphite die, and a 0.2 mm thick graphite foil was used to act as a physical barrier between the graphite die and the powders. $LuPO_4$ pellets were sintered at 1500°C for 5 min with a heating rate of 200°C min^{-1} at 50 MPa. After that, the dense pellets were polished via different sizes of SiC abrasive papers followed by colloidal silica suspension.

2.3 | Phase, thermal stability, and thermal properties characterization

Phase of $LuPO_4$ powders and $LuPO_4$ pellets sintered by SPS was confirmed by the powder X-ray diffraction with a step size of 0.013° by a Panalytical X′ Pert Pro system. The phase stability of $LuPO_4$ powders was measured by a thermogravimetric technique using a TGA-Q50 system (TA instruments). 30 mg of powders were placed in an alumina crucible and heated to 1300°C with a heating rate of 10°C min^{-1} in an Ar atmosphere. The CTE of the sintered pellet was measured by thermal dilatometry (DIL 402 Expedis Supreme, Netzsch). A 13 mm-diameter pellet was heated from 30°C to 1300°C with a heating rate of 10°C min^{-1}. Further, the thermal diffusivity of the sintered $LuPO_4$ pellet was measured using a laser flash apparatus (LFA) (LFA-457, Netzsch). Before this measurement, a 10 mm $LuPO_4$ pellet was polished to a mirror finish and then homogeneously coated with a thin layer of graphite to enhance the laser power absorption and emissivity. The polished and graphite-coated $LuPO_4$ pellet was heated from 30°C to 1000°C with a heating rate of 5°C min^{-1}. The thermal diffusivity was calculated using the Cape–Lehmann method based on a non-linear regression model.[11,36] Density of the sintered $LuPO_4$ pellet was measured by the Archimedes method with distilled water as the immersion medium by using an Adam analytical scale. The specific heat capacity (c_p) was taken from the reference.[37] The thermal conductivity of $LuPO_4$ was calculated using the following equations.[11]

$$k = \alpha \rho c_p, \quad (3)$$

where k, α, ρ and c_p represent the thermal conductivity, thermal diffusivity, density and the specific heat capacity of $LuPO_4$, respectively.

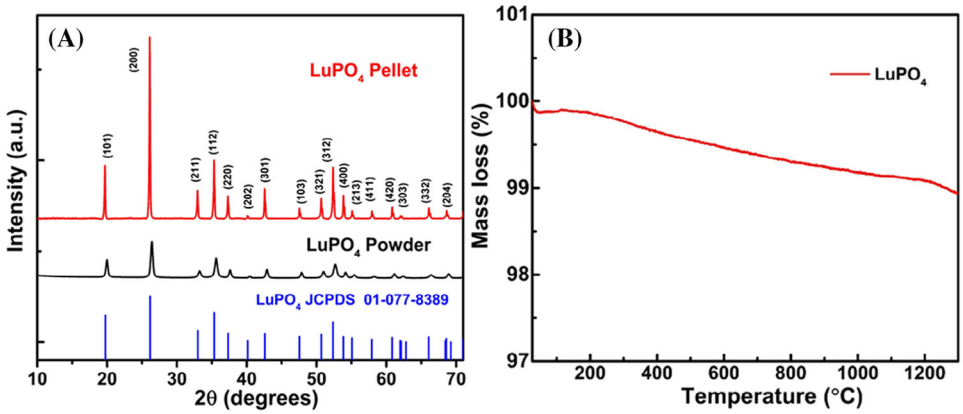

FIGURE 1 (A) X-ray diffraction patterns of $LuPO_4$ powders (black) and sintered pellet (red), and (B) the thermogravimetric analysis (TGA) curve of $LuPO_4$ powders from room temperature to 1300°C.

2.4 | CMAS preparation and corrosion tests

In the present work, CMAS composition is 33CaO–9MgO–$13AlO_{1.5}$–$45SiO_2$ ($C_{33}M_9Al_{13}S_{45}$), which was used in previous studies.[15,20,34,38,39] The starting materials for the synthesis of CMAS are CaO (99.99%, Sigma-Aldrich), MgO (99.99%, Sigma-Aldrich), Al_2O_3 (99.99%, Sigma-Aldrich), and SiO_2 (99.9%, Alfa Aesar) according to the stoichiometric ratio. Then, the mixture was heated to 1300°C with a heating rate of 10°C min^{-1} in a platinum crucible and held for 8 hours, and then quenched in water to produce CMAS glass. These CMAS glass were ground using an agate mortar and pestle into fine powders. The CMAS corrosion tests were performed at 1300°C, 1400°C, and 1500°C. For each test, 30 mg of CMAS powders were placed on top of the sintered pellet with a diameter of 10 mm and heated with a heating rate of 5°C min^{-1} and kept at 1300°C for 5, 45, and 96 hours, and at 1400°C for 5 hours and at 1500°C for 1 and 5 hours. After CMAS testing, the sample's morphology and phase evolution were characterized by optical microscopy, scanning electron microscopy (SEM), and X-ray diffraction (XRD). Cross-section analysis of the samples by SEM was performed in order to observe the reaction layer formation and potential CMAS penetration into the phosphate matrix.

3 | RESULTS AND DISCUSSION

3.1 | XRD and TGA analysis

XRD patterns of the synthesized $LuPO_4$ powders and sintered pellets are shown in Figure 1A. All the diffraction peaks match those of the standard $LuPO_4$ pattern (JCPDS no. 01-077-8389) with a xenotime structure. The stronger intensity of the diffraction peaks for the $LuPO_4$ pellet as compared with the initial powders is attributed to improved crystallinity upon SPS sintering at 1500°C. Typically, phase transition at high temperatures leads to volume change, which could lead to the formation of cracks in the coating materials. The phase stability of $LuPO_4$ was tested by TGA analysis. As shown in Figure 1B, no appreciable mass loss (<1% up to 1300°C) was observed during the heating process, suggesting a high thermal stability of $LuPO_4$.

3.2 | Thermal properties of $LuPO_4$

Thermal expansion of the SPS consolidated pellets was measured by a dilatometry. Figure 2A,B shows the linear expansion rate and the CTE of the $LuPO_4$ pellet, respectively. The CTE value varies from $4.2 \times 10^{-6}°C^{-1}$ to $6.6 \times 10^{-6}°C^{-1}$ from 200°C to 1300°C, which gives an average value $5.69 \times 10^{-6}°C^{-1}$ in this temperature range, close to the CTE value ($5.92 \times 10^{-6}°C^{-1}$) of $LuPO_4$ in a previous study.[15] The CTE values reported for SiC-CMCs vary from $4.5 \times 10^{-6}°C^{-1}$ to $5.5 \times 10^{-6}°C^{-1}$.[40] Hence, $LuPO_4$ displays a CTE close to that of the SiC-CMCs, which is beneficial for reducing thermal stress between ceramic coating and SiC–CMC substrate.

The experimentally-measured CTE values of $LuPO_4$ (shown in Figure 2B) in the temperature range of 200°C–1300°C is lower than that of monosilicates and higher than that of disilicates.[22,41,42] The temperature-dependent thermal diffusivity of the SPS consolidated $LuPO_4$ pellet measured by the LFA technique from room temperature to 1000°C is shown in Figure 2C, and the inset shows the specific heat of $LuPO_4$, taken from a previous study.[37] The thermal conductivity calculated using Equation 3 is shown in Figure 2D. Figure 2C shows that the thermal diffusivity decreases with increasing temperature, reaching a value of around 0.87 mm/s^2 at 1000°C. The thermal conductivity

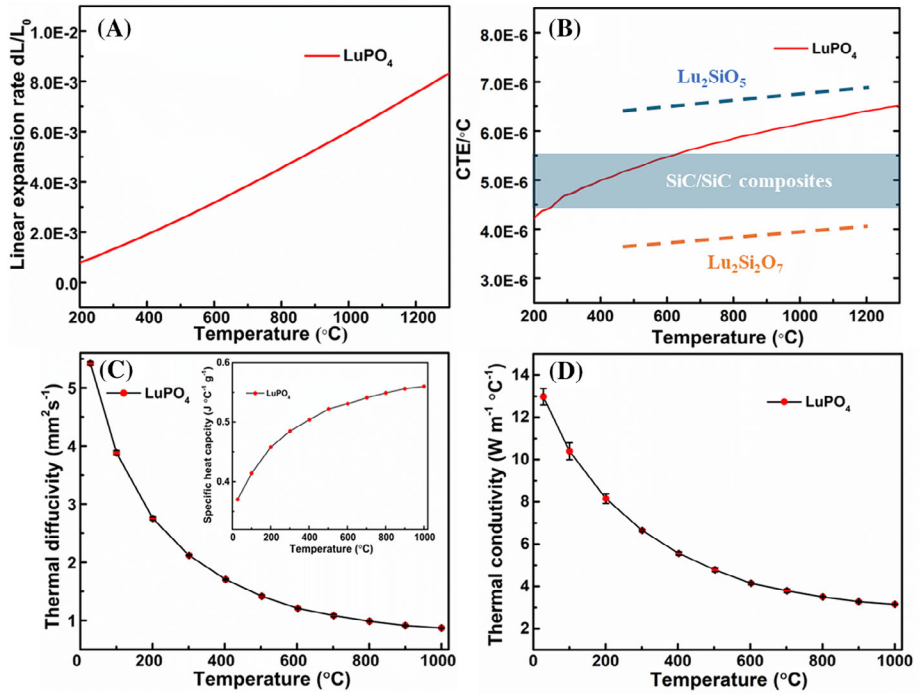

FIGURE 2 (A) Linear expansion rate, and (B) the corresponding coefficient of thermal expansion (CTE) of $LuPO_4$ pellet measured from 200°C to 1300°C, CTEs of Lu_2SiO_5 [22] and $Lu_2Si_2O_7$ [41] (the dashed lines) are also included for comparison. (C) Thermal diffusivity of $LuPO_4$ (inset is the specific heat[37]), and (D) thermal conductivity of $LuPO_4$ pellet as a function of temperature.

also decreases with increasing temperature as heat transfer is dictated by phonon-phonon Umklapp scattering.[26] The thermal conductivity of $LuPO_4$ at 1000°C is 3.15 W $m^{-1}°C^{-1}$, which is between previously reported values of 4.8 W $m^{-1}°C^{-1}$[26] and 2.2 W m^{-1} K^{-1}[15,18,43] for $LuPO_4$ at 1000°C, and higher than that of Lu_2SiO_5 (1.72 W $m^{-1}°C^{-1}$ at 800°C), and $Lu_2Si_2O_7$ (1.8 W $m^{-1}°C^{-1}$ at 1000°C).[15,18,43] The above results show that the thermal conductivity of xenotime rare earth phosphates ($LuPO_4$) is higher than that of mono- and di-silicate in the temperature range of 27°C–1000°C. The thermal conductivity of monazite phosphate is low relative to the xenotime rare earth phosphates due to being more disordered at the intra-atomic length scale than the xenotime structure. This disorder enhances the phonon scattering in the lattice.[27] Further, thermal conductivity depends on the mass of rare earth elements, and its value decreases with the increasing mass of rare earth elements.[26,27] In a previous study[15,26] authors prepared the samples using different techniques, which could be the reason for the deviation of the thermal conductivity value in $LuPO_4$ samples at 1000°C.

3.3 | $LuPO_4$–CMAS interaction at high temperatures

Optical images of the 10 mm diameter $LuPO_4$ pellets after the CMAS reaction at 1300°C, 1400°C, and 1500°C for various durations are shown in Figure 3. After the reaction at 1300°C, most of the CMAS remains on the top of the $LuPO_4$ pellet, indicating negligible penetration and volatilization of CMAS at this temperature. However, after exposure at 1400°C for 5 hours and at 1500°C for 1 hour, the remaining CMAS is reduced significantly, suggesting evaporation or penetration of CMAS into the $LuPO_4$ pellet. After the CMAS reaction at 1500°C for 5 hours, the $LuPO_4$ pellet looks very different as there is no CMAS glass remaining, and most CMAS penetrates throughout the pellet via grain boundaries (see cross-section view later).

The backscattered electron cross-section SEM images of $LuPO_4$ pellets after the CMAS reaction at different temperatures are shown in Figure 4. After the CMAS reaction at 1300°C, a lot of residual CMAS remains on the top of the pellet; however, at 1400 and 1500°C, the molten CMAS penetrates inside the pellet much more as compared to 1300°C. After the CMAS reaction at 1500°C for 5 hours, no residual CMAS can be seen on the top of the $LuPO_4$ pellet.

The XRD diffraction patterns of the $LuPO_4$ surface after CMAS reaction at 1300°C for 5, 45, and 96 h are shown in Figure 5. The primary reaction products are $Ca_8MgLu(PO_4)_7$ and $Lu_2Si_2O_7$, whose reference patterns with PDF cards are included in Figure 5. The XRD pattern after 5-h CMAS corrosion shows the formation of only $Ca_8MgLu(PO_4)_7$ phase. As the corrosion time increases from 5 to 45 and 96 h, more peaks are observed, which match with those of $Lu_2Si_2O_7$. After 45 and 96 h of

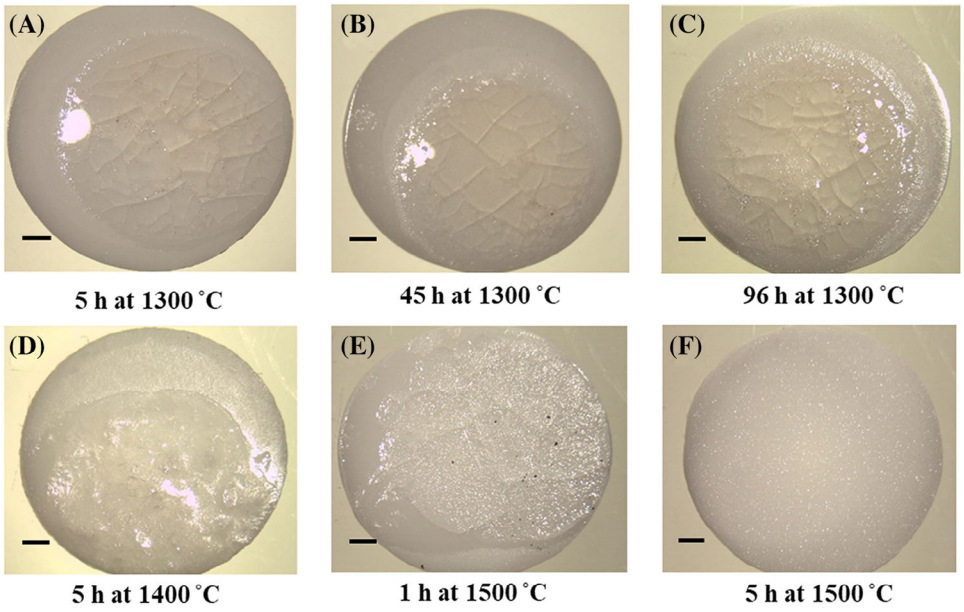

FIGURE 3 Optical images of 10 mm diameter $LuPO_4$ pellets after calcium–magnesium–alumina–silicate (CMAS) reaction at 1300°C for: (A) 5 h, (B) 45 h, and (C) 96 h; (D) at 1400°C for 5 h, (E) at 1500°C for 1 h and (F) at 5 h. The scale bar is 1 mm.

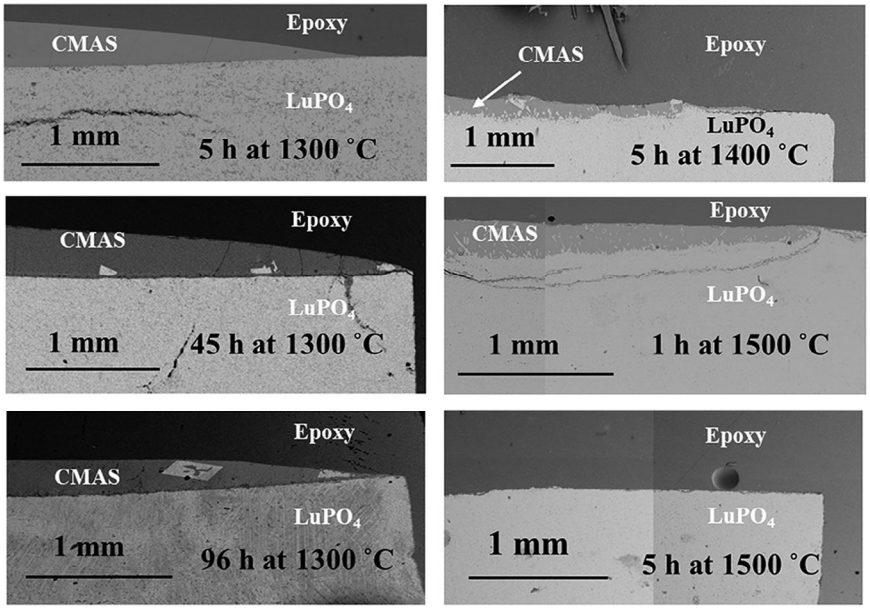

FIGURE 4 Backscattered electron cross-section SEM images of $LuPO_4$ pellets after calcium–magnesium–alumina–silicate (CMAS) reaction at different temperatures for various durations.

CMAS reaction, there may be the presence of $CaAl_2Si_2O_8$, $CaMgSi_2O_6$, and $Ca_2Lu_8(SiO_4)_6O_2$ phases, but their reference XRD patterns overlap with some of the peaks of $Ca_8MgLu(PO_4)_7$, $Lu_2Si_2O_7$ and $LuPO_4$. The presence of $Ca_8MgLu(PO_4)_7$ and $Lu_2Si_2O_7$ indicates that $LuPO_4$ and CMAS react at 1300°C and the reaction mechanism changes with time.

Figure 6 shows the backscattered electron cross-section SEM images and the corresponding energy-dispersive X-ray spectroscopy (EDS) maps and line scan of the $LuPO_4$ pellet after the CMAS reaction at 1300°C for 5 hours. Figure 6A shows the residual CMAS layer, a dense reaction layer, and the bulk $LuPO_4$ pellet. The high-resolution SEM image shows the formation of a reaction layer with an average thickness of approximately 13.3 ± 1.9 μm (see Figure 6B). In both SEM images, there is a large contrast between the reaction layer and the $LuPO_4$ bulk pellet. Further, a slight contrast difference is present in the reaction layer, in which the top of the reaction layer displays a brighter contrast than the bottom reaction layer. Few open

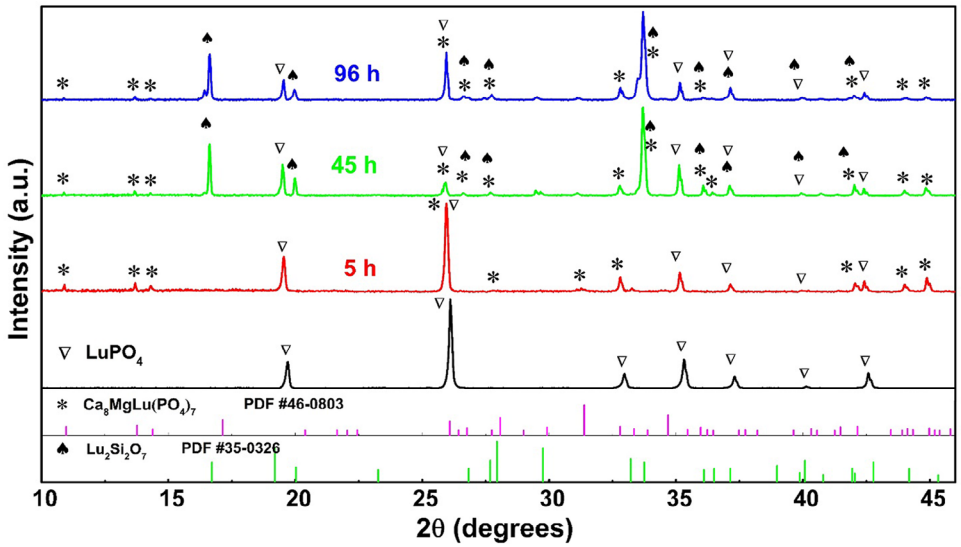

FIGURE 5 X-ray diffraction (XRD) patterns of the $LuPO_4$ surface after calcium–magnesium–alumina–silicate (CMAS) reaction at 1300°C for 5 h (red), 45 h (green), and 96 h (blue).

pores are visible below the continuous and dense reaction layer, as shown in the black circle in Figure 6B, indicating no CMAS between the grains. EDS maps of the $LuPO_4$ pellet after CMAS reaction at 1300°C for 5 h are shown in Figure 6C, which show that no Ca penetrates along the grain boundaries of $LuPO_4$. EDS line scans from region 1, 2 and 3, namely the residual CMAS, reaction layer and $LuPO_4$, are plotted in Figure 6D, showing that negligible amounts of Ca and Si penetrate throughout the $LuPO_4$ matrix. The reaction layer as labeled by region 2 is enriched with Ca and P with a small amount of Lu. In particular, Ca and P exhibit a higher enrichment within the reaction layer compared to its presence within the residual CMAS, as shown in Figure 6D. Further, the concentrations of Ca and P decrease gradually from the bottom to the top of the reaction layer, while Lu and Si show the opposite trend, being higher at the top and decreasing toward the bottom region. The concentration difference results in different contrasts across the reaction layer. The Ca- and P-enriched phase is consistent with the observation in the XRD pattern shown in Figure 5, which clearly indicates the formation of $Ca_8MgLu(PO_4)_7$ phase. In the residual CMAS region (region 1) (as shown in Figure 6D), a large amount of Ca, and Si exist with moderate amounts of P, and Lu, indicating the dissolution of $LuPO_4$ in molten CMAS. The noticeable contrast difference in Ca and Si levels on either side of the reaction layer suggests that the penetration of CMAS is halted to a certain extent by the continuous and dense reaction layer of $Ca_8MgLu(PO_4)_7$.[15]

Figure 7A,C shows the backscattered electron cross-section SEM images of $LuPO_4$ pellets after the CMAS corrosion test at 1300°C for 45 and 96 h, respectively. Figure 7B,D are the high-resolution SEM images from the area highlighted by the red boxes in Figure 7A,C. Similar to the 5-h CMAS corrosion, a dense and continuous reaction layer forms between $LuPO_4$ and residual CMAS in both cases. However, the reaction layer consists of two regions with different contrasts, i.e., the top part is brighter as compared to the bottom part. This is likely due to the concentration difference of Lu, similar to the 5-h corrosion tested sample. After 45 h and 96 h at 1300°C, the average thickness of the reaction layer is 33.6 ± 5.7 μm and 44.7 ± 6.2 μm, respectively. After reaction for 96 hours, white spots are present in the dense reaction layer and on top of the reaction layer (Figure 7C), which are not observed in the 5- and 45-h reaction tests, and confirmed to be $Lu_2Si_2O_7$ as evidenced by XRD patterns shown in Figure 5. The EDS maps of $LuPO_4$ pellet after CMAS reaction at 1300°C for 45 hours are shown in Figure 7E. The line scan along the vertical yellow line (in Figure 7F) shows that the reaction layer is highly enriched with Ca and P, and a relatively small amount of Lu and Si are present. Similar to the 5-h corrosion test, the concentrations of Ca and P are higher at the bottom of the reaction layer, decreasing gradually to the top of the reaction layer. In contrast, the concentration of Lu and Si is higher at the top of the reaction layer, decreasing towards the bottom of the reaction layer. The open pores are clearly visible below the continuous and dense reaction layer, as shown in the black circles in Figure 7B,D, suggesting no CMAS between the grains. This indicates that the dense and continuous reaction layer slows down the CMAS penetration to a certain extent in the bulk $LuPO_4$ pellet. After 45 and 96 h of CMAS corrosion, the $LuPO_4$ substrate maintains its structural integrity beneath the reaction layer, suggesting the high resistance of $LuPO_4$ against CMAS corrosion at 1300°C.

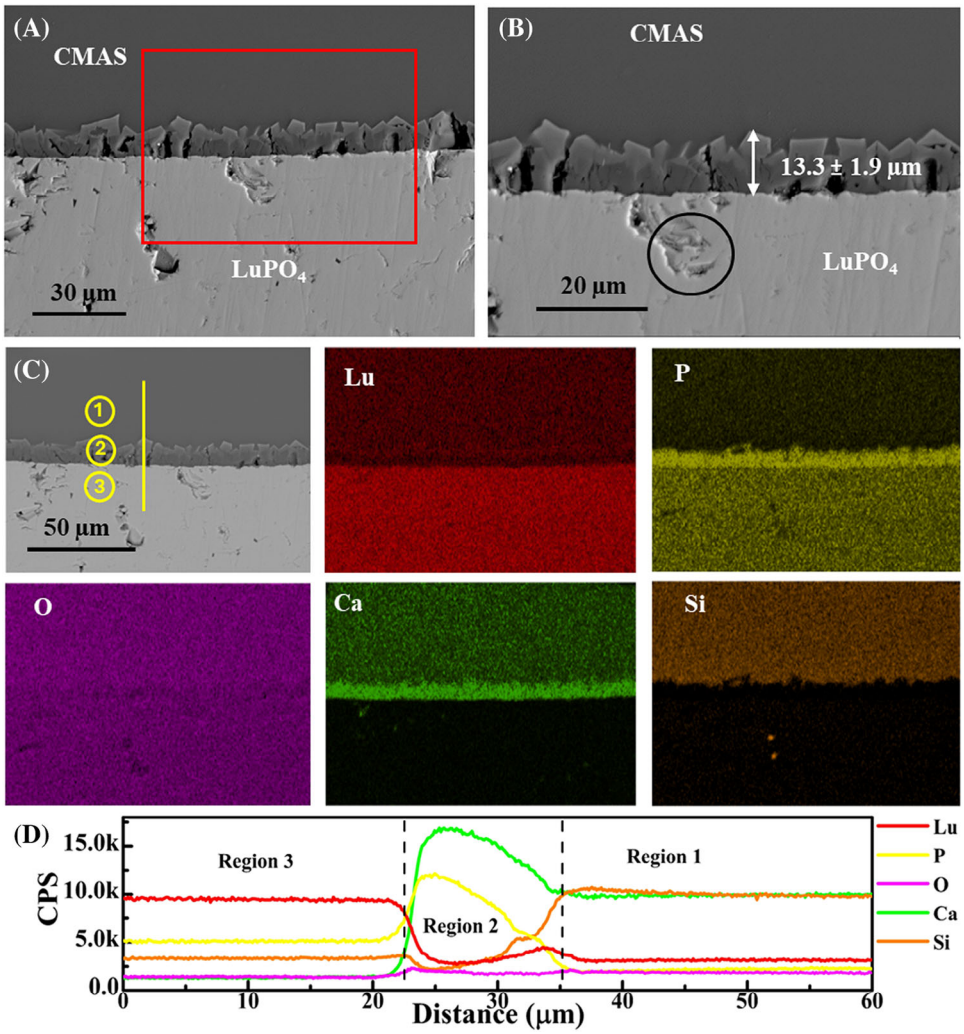

FIGURE 6 (A) Low and (B) high magnifications (area marked by the red box in (A)) of SEM backscattered electron images of the cross-section of the $LuPO_4$ pellet after calcium–magnesium–alumina–silicate (CMAS) reaction at 1300°C for 5 h, and (C) energy-dispersive X-ray spectroscopy (EDS) elemental maps, and (D) EDS scan along the vertical yellow line traversing regions 1, 2 and 3 marked by yellow circles in (C).

The thickness of the reaction layer gradually increases with the reaction time, as shown in Figures 6B, and 7B,D. The growth of the interfacial layer could be due to the reaction between the phosphate matrix and the molten CMAS penetrated through the dense reaction layer with reduced kinetics, or at the expense of the CMAS already penetrated during the shorter duration at the beginning of the reaction. At 1300°C, the reaction layer thickness grows with time. However, the growth rate of the reaction layer reduces with increasing corrosion durations. This is substantiated by a 29% reduction in growth observed from 45 to 96 h when compared to the growth between 5 and 45 h. This demonstrates that the compact and continuous reaction layer can impede the penetration of CMAS into $LuPO_4$. The average thickness of the reaction layer between $LuPO_4$–CMAS interaction at 1300°C is plotted against the square root of time in Figure 8. A linear relation between the reaction layer and the square root of time can be identified with a rate constant of $4.2 \pm 0.2\ \mu m\ h^{-0.5}$. This linear correlation indicates that a diffusion-controlled mechanism likely governs the interfacial layer's growth during the CMAS reaction with the phosphate matrix. Previously, the rate constants for the interfacial layer growth in $LuPO_4$ and $YbPO_4$ after reaction with the same composition of CMAS at 1300°C were reported to be 5.3 and $5.0\ \mu m\ h^{-0.5}$, respectively.[15,31]

To further evaluate the potential of $LuPO_4$ as an EBC at higher temperatures and understand the reaction mechanisms, CMAS-$LuPO_4$ interaction behavior was studied at 1400°C and 1500°C. Figure 9 shows the XRD patterns for the $LuPO_4$ pellet after the CMAS reaction at 1400°C for 5 h and 1500°C for 1 h and 5 h, respectively. After 5 h of CMAS reaction at 1400°C, the diffraction peaks indicate the formation of $Lu_2Si_2O_7$, and $CaMgSi_2O_6$. However, after 1 hour

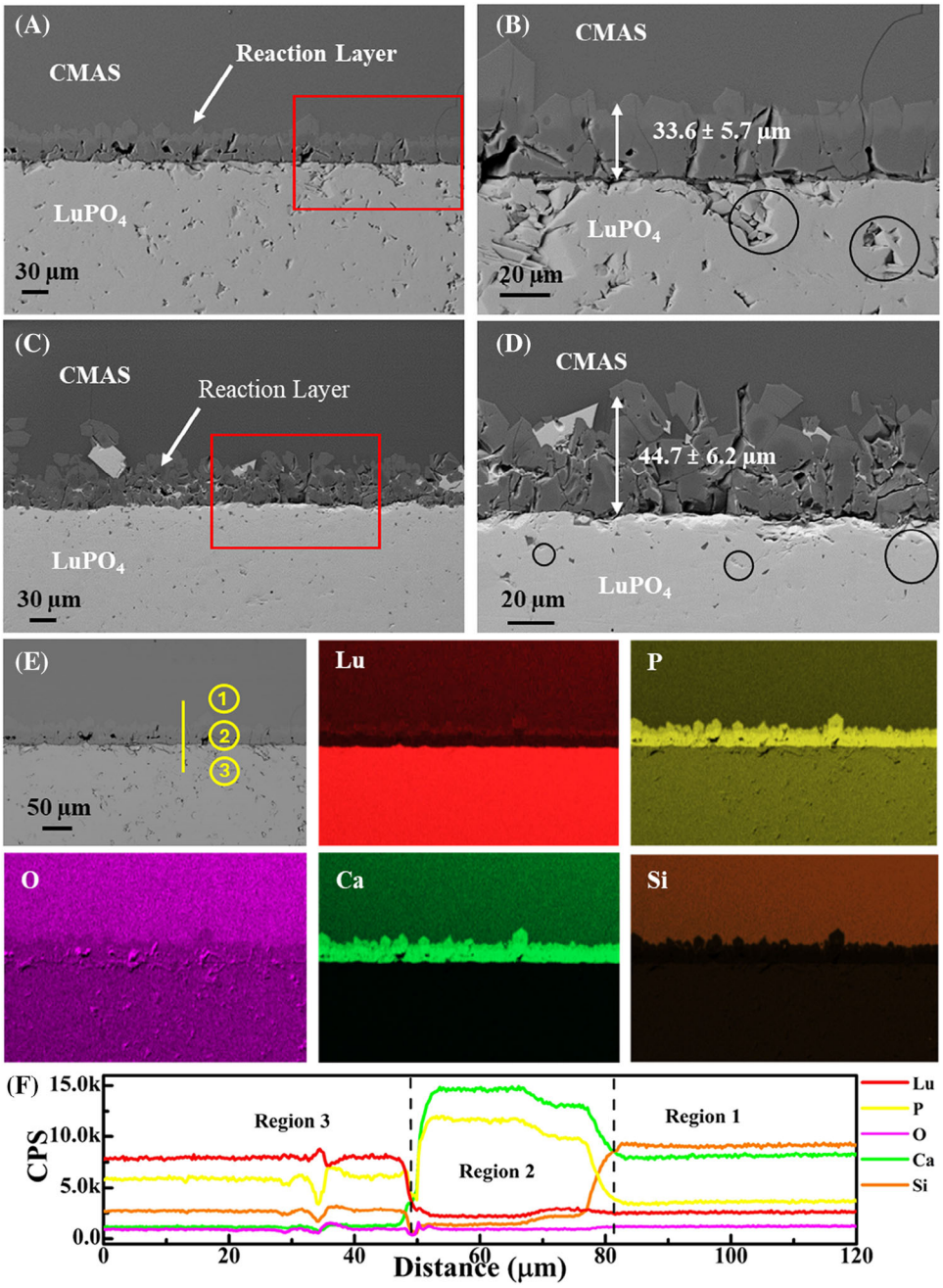

FIGURE 7 Backscattered electron SEM cross-section images of $LuPO_4$ pellets after calcium–magnesium–alumina–silicate (CMAS) reaction at 1300°C for: (A) 45 h and (C) 96 h, and high-resolution SEM image and reaction layer thickness (B) for 45 h and (D) for 96 h, (E) energy-dispersive X-ray spectroscopy (EDS) elemental maps of $LuPO_4$ pellets after CMAS reaction at 1300°C for 45 h, and (F) EDS scan along the vertical yellow line traversing regions 1, 2 and 3 marked by yellow circles in (E).

at 1500°C, the XRD pattern shows small extra peaks apart from pure $LuPO_4$ and these small peaks are attributed to $CaMgSi_2O_6$ (the intensity of peaks multiplied by 5 to make those small peaks visible). After 5 h at 1500°C, no extra peaks from any secondary phases can be observed in the XRD pattern. Different phase behaviors suggest a change in the reaction mechanisms between $LuPO_4$ and CMAS at 1300°C, 1400°C, and 1500°C with time, which will be discussed in detail later.

The backscattered electron cross-sectional SEM images of $LuPO_4$–CMAS interface at 1400°C for 5 h shows no reaction layer formed (see Figure 10A), consistent with the XRD pattern in Figure 9 without the formation of $Ca_8MgLu(PO_4)_7$ phase. As there is no reaction layer at

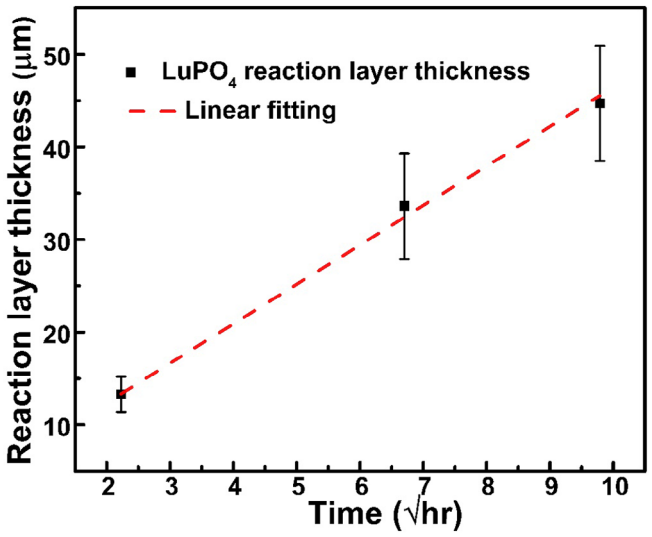

FIGURE 8 Average reaction layer thickness versus the square root of time for $LuPO_4$–CMAS (calcium–magnesium–alumina–silicate) interaction at 1300°C.

the CMAS/$LuPO_4$ interface to halt the CMAS penetration, molten CMAS infiltrates the bulk $LuPO_4$ pellet via the grain boundaries, as shown in the regions marked by red circles in Figure 10A. A higher magnification cross-sectional SEM image in Figure 10B shows dendritic-like grain growth over the entire residual CMAS layer. The CMAS penetration is not restricted to a certain depth; it penetrates to the bottom of the $LuPO_4$ pellet, as shown in Figure 10C. The EDS elemental maps of the cross-section of the pellet after exposure at 1400°C for 5 h (see Figure 10D) show that the constituent elements (Ca, Si) diffuse inside the $LuPO_4$ pellet. The XRD/EDS analysis reveals that there is a mixture of $Lu_2Si_2O_7$, and $CaMgSi_2O_6$ phases in the $LuPO_4$/CMAS interfacial region.

Figure 11A,C shows the backscattered electron cross-sectional SEM images of the CMAS/$LuPO_4$ interface after the CMAS reaction at 1500°C for 1 and 5 h, respectively. No reaction layer forms in both samples, which can be further confirmed by the XRD patterns (Figure 9). In the case of 1 hour reaction at 1500°C, a crack occurs just underneath the CMAS due to the thermal stress in the CMAS/$LuPO_4$ interface,[20] as shown in Figures 11A, and S1. Figure 11B is a high-resolution SEM image from the red box highlighted in Figure 11A, showing that molten CMAS penetrates inside the $LuPO_4$ bulk pellet via the grain boundaries. Similar results are observed in the sample tested at 1500°C for 5 h, and no residual CMAS remains, as shown in Figures 11C,D and S2. The EDS elemental maps (Figure 11E) further confirm the presence of CMAS in the bulk pellet. However, there is no volumetric swelling in the bulk $LuPO_4$, and no new phase change is observed in XRD, as shown in Figure 9. Ca and Si are predominantly present between the pellet grains.

3.4 | CMAS corrosion mechanisms of $LuPO_4$ at 1300°C, 1400°C and 1500°C

The dense layer formation at the interface of CMAS/$LuPO_4$ observed at 1300°C mainly consists of $Ca_8MgLu(PO_4)_7$, which has a very high melting point that halts the CMAS penetration inside the $LuPO_4$ pellet. At temperatures above the melting temperature (~1235°C) of CMAS,[15] $LuPO_4$ dissolves into the molten glass and reacts with the constituent elements, resulting in the crystallization of $Ca_8MgLu(PO_4)_7$ and di-silicate ($Lu_2Si_2O_7$) phases.[15] At starting, CMAS reacted with $LuPO_4$ and formed $Ca_8MgLu(PO_4)_7$ according to Equation 4,[31] and this phase was observed in XRD for all three durations at 1300°C.

$$7LuPO_4 + 8CaO + MgO \rightarrow Ca_8MgLu(PO_4)_7 + \text{Lu-Si enriched CMAS glass} \quad (4)$$

The EDS image shows the presence of rare earth elements, i.e., Lu, in the residual CMAS layer after the formation of Ca- and P-enriched $Ca_8MgLu(PO_4)_7$ phase. Prolonged durations of CMAS reaction result in the formation of a disilicate phase ($Lu_2Si_2O_7$) along with $Ca_8MgLu(PO_4)_7$, as shown in XRD results. In the prolonged corrosion period (for 45 and 96 h), the local Lu and Si in the residual CMAS glass accumulate to a certain value and precipitate into the $Lu_2Si_2O_7$ phase.[15,31] This compound emerges both at the uppermost surface of the reaction layer and within the residual CMAS. Because the interfacial region contains the highest concentration of initially dissolved Lu and P, $Ca_8MgLu(PO_4)_7$ precipitation occurs in the closest proximity to the bulk pellet, and the dense layer formed could act as a barrier against further CMAS interaction and infiltration.[11] In other studies, similar behaviors were also observed in $LuPO_4$ and $YbPO_4$ after CMAS interaction at 1300°C.[15,31] Once the concentrations of Lu and Si within the CMAS glass reach a specific threshold, the byproduct crystallization of $Lu_2Si_2O_7$ occurs, leading to its precipitation as seen in the XRD patterns after 45 and 96 h of CMAS reaction at 1300°C in Figure 5. It can also be possible that other byproducts such as $CaAl_2Si_2O_8$ may form when there is some local excess Al_2O_3 in the molten CMAS after CaO, MgO and SiO_2 are consumed to form $Ca_8MgLu(PO_4)_7$ and $Lu_2Si_2O_7$.[15]

After $LuPO_4$ is exposed to CMAS at 1300°C, a continuous, thick, and dense reaction layer form, which mainly consists of $Ca_8MgLu(PO_4)_7$ phase. For mono- or di-silicates, the major phase formed upon the CMAS reaction is $Ca_2RE_8(SiO_4)_6O_2$.[19,20,35,44] Notably, a significantly reduced quantity of Lu is required for the formation of $Ca_8MgLu(PO_4)_7$ phase compared to $Ca_2Lu_8(SiO_4)_6O_2$

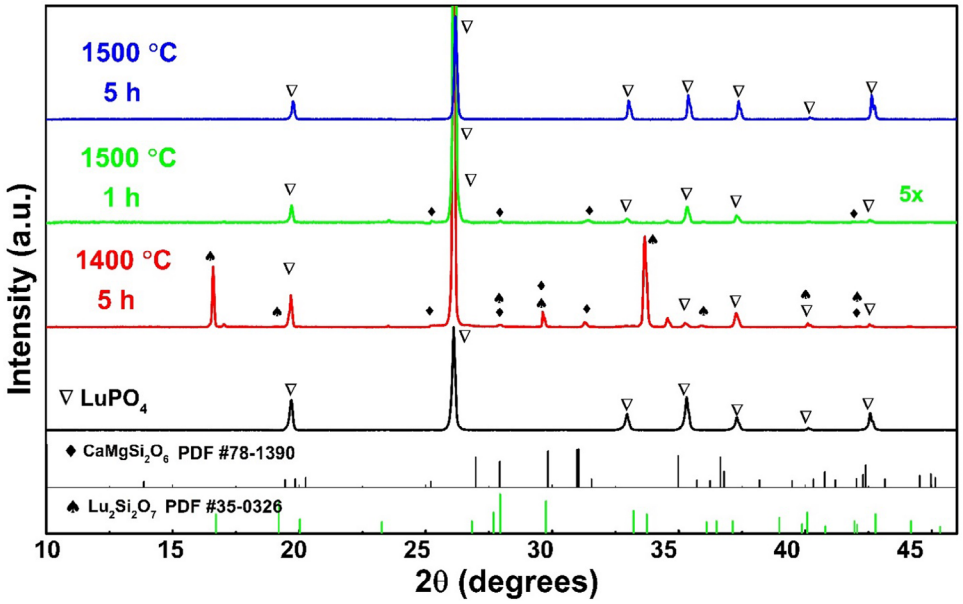

FIGURE 9 X-ray diffraction (XRD) patterns of $LuPO_4$ pellets after calcium–magnesium–alumina–silicate (CMAS) reaction at 1400°C for 5 h (red) and 1500°C for 1 h (green) and 5 h (blue).

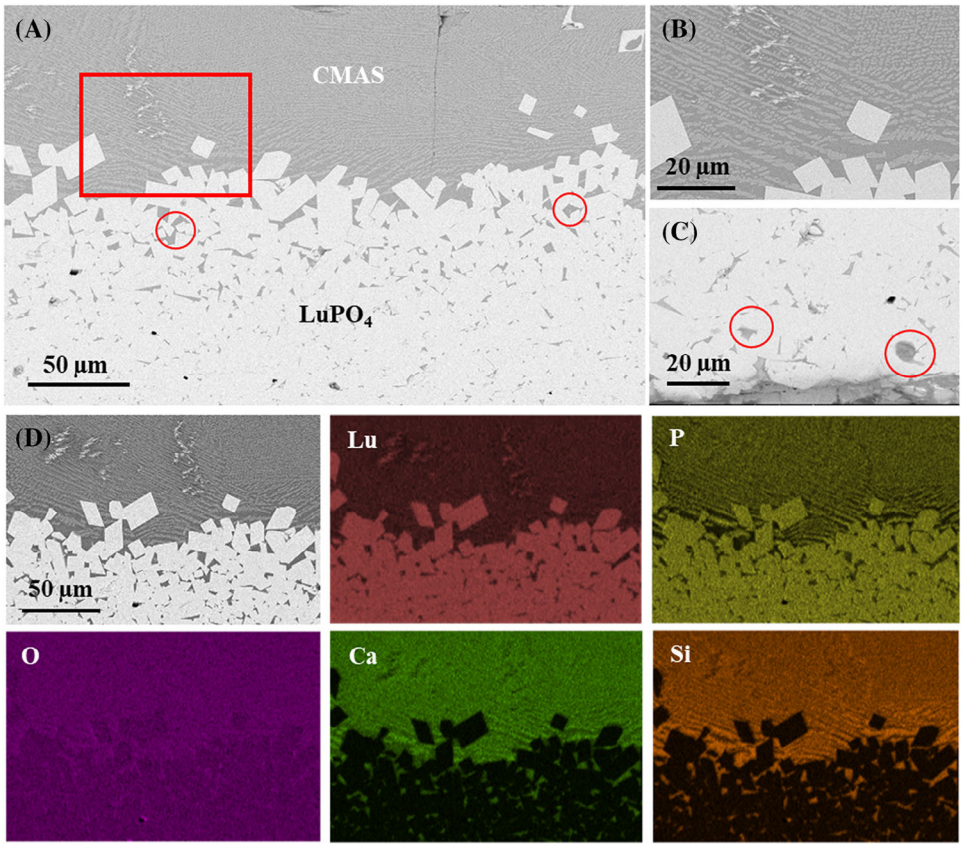

FIGURE 10 (A) A backscattered electron SEM image of the cross-section of $LuPO_4$ pellets after CMAS reaction at 1400°C for 5 h, (B) a SEM image at a higher magnification of the area marked by the red box in (A), (C) a cross-section SEM image of $LuPO_4$ pellet's bottom, and (D) EDS elemental maps of $LuPO_4$ reaction with calcium–magnesium–alumina–silicate (CMAS) for 5 h at 1400°C.

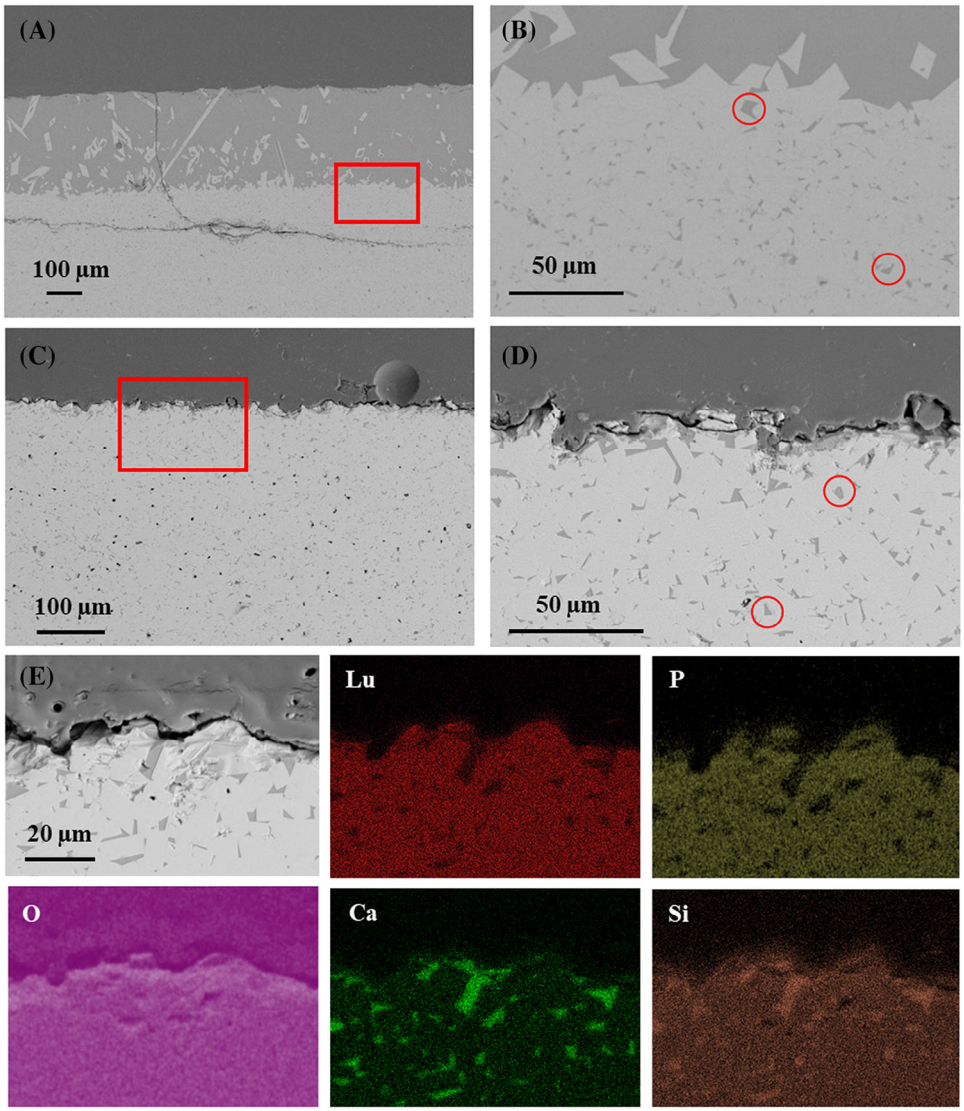

FIGURE 11 Backscattered electron SEM images of $LuPO_4$ pellets after calcium–magnesium–alumina–silicate (CMAS) reaction at 1500°C for (A and B) 1 h, (C and D) 5 h, and (E) EDS elemental maps of $LuPO_4$ reaction with CMAS for 5 h at 1500°C.

phase (a 32-fold difference based on the Ca:RE ratio).[15] This means much more corrosion and dissolution of Lu are required from the silicate matrix to form the Lu-enriched oxyapatite. Further, in the $LuPO_4$–CMAS reaction, the formation of $Ca_8MgLu(PO_4)_7$ phase reduces the amount of CaO and MgO in the residual CMAS glass by forming $Ca_8MgLu(PO_4)_7$, and due to that, the viscosity of melt residual CMAS glass decreases and lowers the penetration ability of CMAS glass in the bulk pellets compared to the CMAS-silicate corrosion reaction.[31] The rapid formation of a dense Ca-enriched interface layer in $LuPO_4$ prevents further penetration of molten CMAS and well maintains the pellet integrity without volumetric swelling, clearly indicating that the resistance of $LuPO_4$ to CMAS is higher than that of mono- and di-silicates at 1300°C.[24,25,33,39,45]

At 1400°C and 1500°C, no reaction layers are observed at the interface of $LuPO_4$/CMAS. At 1400°C, XRD/EDS analysis indicates the presence of a mixture of $Lu_2Si_2O_7$ and $CaMgSi_2O_6$ phases in the residual CMAS. The disilicate phase forms due to the precipitations of the Lu and Si in the molten CMAS. At the higher temperature of 1500°C for 1 h, XRD shows the presence of $CaMgSi_2O_6$ along with $LuPO_4$. After 5 h of CMAS corrosion at 1500°C, CMAS did not interact with $LuPO_4$; instead, it passed through the $LuPO_4$ bulk pellets. This behavior may be attributed to the low viscosity of molten CMAS at higher temperatures.

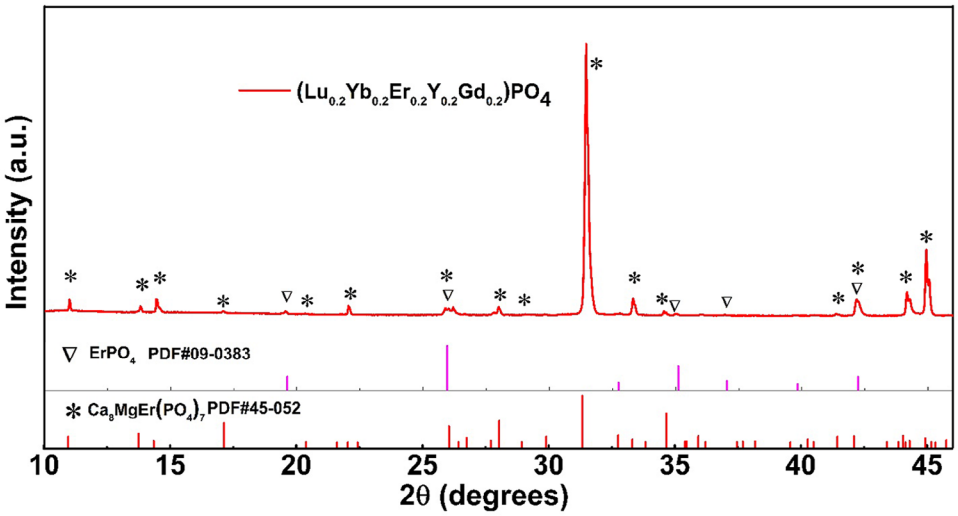

FIGURE 12 X-ray diffraction (XRD) patterns of $(Lu_{0.2}Yb_{0.2}Er_{0.2}Y_{0.2}Gd_{0.2})PO_4$ after calcium–magnesium–alumina–silicate (CMAS) reaction at 1400°C for 5 h.

3.5 | Effects of temperature on CMAS corrosion and a comparison of CMAS corrosion tests on single component and multicomponent phosphates

Figures 9–11 show that at higher temperatures of 1400°C and 1500°C, there is no formation of the reaction layer, and molten CMAS infiltrates inside the $LuPO_4$ bulk pellet via grain boundaries. XRD analysis shows the formation of $Lu_2Si_2O_7$, and $CaMgSi_2O_6$ phases after $LuPO_4$–CMAS interaction at 1400°C. At 1500°C for 1 and 5 h, $LuPO_4$–CMAS interactions show the formation of the $CaMgSi_2O_6$ phase and pure $LuPO_4$, respectively. Currently, no CMAS corrosion studies on single component rare earth phosphates at 1400°C and 1500°C are available, apart from one multicomponent phosphate $(Lu_{0.2}Yb_{0.2}Er_{0.2}Y_{0.2}Gd_{0.2})PO_4$ studied by Bryce et al. (at 1300°C, 1400°C, and 1500°C).[11] However, the abovementioned study tested with different CMAS ($40CaO–5MgO–5AlO_{1.5}–50SiO_2$) compositions. The compositions of CMAS glass can give different corrosion products and reaction layer thickness. Hence, for a direct comparison of CMAS corrosion tests on a single component and multicomponent phosphates, we exposed $(Lu_{0.2}Yb_{0.2}Er_{0.2}Y_{0.2}Gd_{0.2})PO_4$ to the same CMAS ($33CaO–9MgO–13AlO_{1.5}–45SiO_2$) at 1400°C for 5 h as for $LuPO_4$. The synthesis, characterization, and CMAS corrosion (with a different composition) of $(Lu_{0.2}Yb_{0.2}Er_{0.2}Y_{0.2}Gd_{0.2})PO_4$ can be found in our previous study.[11] Figure 12 shows the XRD pattern of the surface layer of $(Lu_{0.2}Yb_{0.2}Er_{0.2}Y_{0.2}Gd_{0.2})PO_4$ after CMAS corrosion at 1400°C for 5 hours, in which $Ca_8MgRE(PO_4)_7$ phase along with the bulk material $REPO_4$ are observed. While in Bryce et al.'s study of $(Lu_{0.2}Yb_{0.2}Er_{0.2}Y_{0.2}Gd_{0.2})PO_4$–CMAS ($40CaO–5MgO–5AlO_{1.5}–50SiO_2$) reaction at 1400°C for 5 h, $Ca_8MgRE(PO_4)_7$ and cristobalite silica were observed. Due to the reduced SiO_2 content in the CMAS used in the current work, the amount of SiO_2 in the residual CMAS is too low for the precipitation of the cristobalite phase.[11] The above results show that depending on the CMAS composition, different reaction products can be observed after CMAS corrosion tests. This is very reasonable but poses significant challenges in understanding the CMAS corrosion resistance of EBCs, as CMAS composition can vary substantially at different geologic locations.

Figure 13 shows backscattered electron SEM images of $(Lu_{0.2}Yb_{0.2}Er_{0.2}Y_{0.2}Gd_{0.2})PO_4$–CMAS interface after the reaction at 1400°C for 5 h, in which a dense reaction layer of $Ca_8MgRE(PO_4)_7$ of 23.8 ± 7.2 μm in thickness can be clearly seen. This is completely different from the $LuPO_4$–CMAS reaction at 1400°C for 5 h (shown in Figure 10), where no reaction layer is formed. Figure 13C,D shows a clear infiltration front, where the CMAS melt penetrates past the reaction layer, but stops somewhere within the bulk pellet, as indicated by the red dashed line below which the darker areas between grains are no longer visible. Red circles in Figure 13B represent the presence of CMAS below the reaction layer. On the contrary, a complete CMAS penetration is observed in the $LuPO_4$–CMAS reaction at 1400°C for 5 h. The above observations show that multicomponent rare earth phosphate has a better CMAS corrosion resistance than single component rare earth phosphate at higher temperatures.

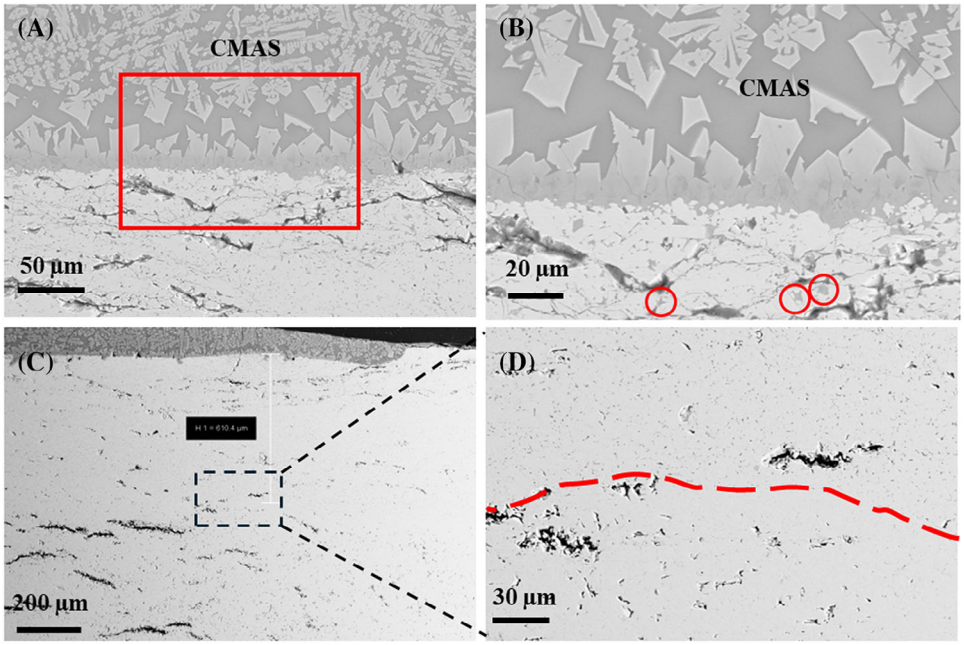

FIGURE 13 Backscattered electron SEM images of the cross-section of $(Lu_{0.2}Yb_{0.2}Er_{0.2}Y_{0.2}Gd_{0.2})PO_4$ after calcium–magnesium–alumina–silicate (CMAS) interaction at 1400°C for 5 h: (A) low and (B) high magnification (area marked by the red box in (A)), (C) low and (D) high magnification images of CMAS penetrated bulk pellet of $(Lu_{0.2}Yb_{0.2}Er_{0.2}Y_{0.2}Gd_{0.2})PO_4$.

CMAS corrosion tests of mono-, di- and multicomponent silicates at high temperatures (1300°C–1500°C) have been previously studied.[11,19,34,35] For example, Tian et al. conducted a CMAS test of γ-$Y_2Si_2O_7$, β-$Yb_2Si_2O_7$, and β-$Lu_2Si_2O_7$ at 1300°C and 1500°C for 50 h. At 1300°C, $RE_2Si_2O_7$ dissolved into CMAS and formed a thick reaction layer. However, at 1500°C molten CMAS penetrated through $RE_2Si_2O_7$ via grain boundaries and blister cracks and pores were observed throughout the pellet.[34] Sun et al. reported CMAS corrosion test of β-$(Er_{0.25}Tm_{0.25}Yb_{0.25}Lu_{0.25})_2Si_2O_7$ at 1500°C for 4 and 50 h. They found oxyapatite phase ($Ca_2RE_8(SiO_4)_6O_2$) formation after CMAS reaction after 50 h, which was not observed in single component disilicates at 1500°C. From the observation in rare earth disilicates and phosphates, multicomponent materials generally show better CMAS corrosion resistance at high temperatures as compared to single component counterparts, likely due to the enhancement of grain boundary stability and slower dissolution rate of multicomponent materials into molten CMAS.[35] In rare earth phosphates studied in this work, there was no volumetric swelling after the CMAS reaction at high temperatures, different from that observed in silicates.[34,38,39] This study shows that single component rare earth phosphates like $LuPO_4$ can be promising EBC materials for SiC-based CMCs up to 1300°C, and the design of multicomponent rare earth phosphates is needed for EBC applications at higher temperatures.

4 | CONCLUSIONS

In this work, we synthesized $LuPO_4$ powders via the chemical coprecipitation technique and consolidated them into dense pellets using SPS, and studied their thermal stability, phase, and thermal properties. $LuPO_4$ shows a high phase stability at high temperatures and has an average CTE value close to that of SiC-based CMCs. Resistance of $LuPO_4$ against CMAS corrosion was systematically investigated at 1300°C for 5, 45, and 96 h, and at 1400°C for 5 h, and at 1500°C for 1 and 5 h. At 1300°C, molten CMAS interacts with $LuPO_4$, forming a dense and continuous $Ca_8MgLu(PO_4)_7$ reaction layer, preventing the CMAS penetration below the reaction layer. The reaction layer thickness is observed to increase with reaction time at 1300°C, and a diffusion-controlled mechanism is identified for the growth of the interfacial layer. At 1400°C and 1500°C, the molten CMAS fully infiltrates into the bulk pellet via grain boundaries without forming a reaction layer, but no volumetric swelling and pore formation are observed. Compared to $LuPO_4$, improved CMAS corrosion resistance at 1400°C was observed in multicomponent rare earth phosphate $(Lu_{0.2}Yb_{0.2}Er_{0.2}Y_{0.2}Gd_{0.2})PO_4$ due to the enhanced grain boundary stability and slower dissolution rate into molten CMAS. Further studies are warranted to develop multicomponent rare earth phosphates as potential EBCs for higher-temperature applications.

ACKNOWLEDGMENTS

This work was supported by the National Science Foundation under Award DMREF-2119423.

CONFLICT OF INTEREST STATEMENT

The authors declare no conflicts of interest.

ORCID

Bishnu Pada Majee https://orcid.org/0000-0002-1500-9580
Liping Huang https://orcid.org/0000-0001-6121-5054
Jie Lian https://orcid.org/0000-0002-9060-8831

REFERENCES

1. Padture NP. Advanced structural ceramics in aerospace propulsion. Nat Mater. 2016;15(8):804–89. https://doi.org/10.1038/nmat4687
2. Stokes JL, Harder BJ, Wiesner VL, Wolfe DE. High-Temperature thermochemical interactions of molten silicates with $Yb_2Si_2O_7$ and $Y_2Si_2O_7$ environmental barrier coating materials. J Eur Ceram Soc. 2019;39(15):5059–67. https://doi.org/10.1016/j.jeurceramsoc.2019.06.051
3. Poerschke DL, Jackson RW, Levi CG. Silicate deposit degradation of engineered coatings in gas turbines: progress toward models and materials solutions. Annu Rev Mater Res. 2017;47:297. https://doi.org/10.1146/annurev-matsci-010917-105000
4. Opila EJ, Robinson RC, Verrilli MJ. Borosilicate glass-induced fiber degradation of sic/bn/sic composites exposed in combustion environments. Int J Appl Ceram Technol. 2016;13(3):434–42. https://doi.org/10.1111/ijac.12499
5. Chen HF, Zhang C, Liu YC, Song P, Li W, Yang G, et al. Recent progress in thermal/environmental barrier coatings and their corrosion resistance. Rare Metals. 2020;39(5):498–512. https://doi.org/10.1007/s12598-019-01307-1
6. Wang X, Gao X, Zhang Z, Cheng L, Ma H, Yang W. Advances in modifications and high-temperature applications of silicon carbide ceramic matrix composites in aerospace: a focused review. J Eur Ceram Soc. 2021;41(9):4671–88. https://doi.org/10.1016/j.jeurceramsoc.2021.03.051
7. Park MS, Gu J, Lee H, Lee SH, Feng L, Fahrenholtz WG. C_f/SiC ceramic matrix composites with extraordinary thermomechanical properties up to 2000°C. Nanomaterials. 2024;14(1):72–85. https://doi.org/10.3390/nano14010072
8. Tejero-Martin D, Bennett C, Hussain T. A review on environmental barrier coatings: history, current state of the art and future developments. J Eur Ceram Soc. 2021;41(3):1747–68. https://doi.org/10.1016/j.jeurceramsoc.2020.10.057
9. Eaton HE, Linsey GD. Accelerated oxidation of SiC CMC's by water vapor and protection via environmental barrier coating approach. J Eur Ceram Soc. 2002;22:2741–47. https://doi.org/10.1016/S0955-2219(02)00141-3 www.elsevier.com/locate/jeurceramsoc
10. Zhang J, Liu R, Jian Y, Wan F, Wang Y. Degradation mechanism of SiC_f/SiC composites after long-time water vapor and oxygen corrosion at 1300°C. Corros Sci. 2022;197:110099–109. https://doi.org/10.1016/j.corsci.2022.110099
11. Bryce K, Shih YT, Huang L, Lian J. Calcium-Magnesium-aluminosilicate (CMAS) corrosion resistance of high entropy rare-earth phosphate $(Lu_{0.2}Yb_{0.2}Er_{0.2}Y_{0.2}Gd_{0.2})PO_4$: a novel environmental barrier coating candidate. J Eur Ceram Soc. 2023;43:6461–72. https://doi.org/10.1016/j.jeurceramsoc
12. Liu B, Liu Y, Zhu C, Xiang H, Chen H, Sun L, et al. Advances on strategies for searching for next generation thermal barrier coating materials. J Mater Sci Technol. 2019;35(5):833–51. https://doi.org/10.1016/j.jmst.2018.11.016
13. Zhang P, Duan X, Xie X, Ding D, Yang T, Hou X, et al. Xenotime-type high-entropy $(Dy_{1/7}Ho_{1/7}Er_{1/7}Tm_{1/7}Yb_{1/7}Lu_{1/7}Y_{1/7})PO_4$: A promising thermal/environmental barrier coating material for SiC_f/SiC ceramic matrix composites. J Adv Ceram. 2023;12(5):1033–45. https://doi.org/10.26599/JAC.2023.9220736
14. Qian B, Wang Y, Zu J, Xu K, Shang Q, Bai Y. A review on multicomponent rare earth silicate environmental barrier coatings. J Mater Sci Technol. 2024;29:1231–43. https://doi.org/10.1016/j.jmrt.2024.01.170
15. Hu X, Xu F, Li K, Zhang Y, Xu Y, Zhao X. Thermal properties and calcium-magnesium-alumina-silicate (CMAS) resistance of $LuPO_4$ as environmental barrier coatings. J Eur Ceram Soc. 2020;40(4):1471–7. https://doi.org/10.1016/j.jeurceramsoc.2019.11.018
16. Bryce K, Majee BP, Huang L, Lian J. A systematic study of thermomechanical properties and calcium-magnesium-aluminosilicate (CMAS) corrosion of multicomponent rare-earth phosphates. J Adv Ceram. 2024; https://doi.org/10.26599/JAC.2024.9220978
17. Poerschke DL, Hass DD, Eustis S, Seward GGE, Van Sluytman JS, Levi CG. Stability and CMAS resistance of ytterbium-silicate/hafnate EBCs/TBC for SiC composites. J Am Ceram Soc. 2015;98(1):278–86. https://doi.org/10.1111/JACE.13262
18. Tian Z, Zheng L, Li Z, Li J, Wang J. Exploration of the low thermal conductivities of γ- γ-$Y_2Si_2O_7$, β-$Y_2Si_2O_7$, β-$Yb_2Si_2O_7$, and β-$Lu_2Si_2O_7$ as novel environmental barrier coating candidates. J Eur Ceram Soc. 2016;36(11):2813–23. https://doi.org/10.1016/j.jeurceramsoc.2016.04.022
19. Turcer LR, Krause AR, Garces HF, Zhang L, Padture NP. Environmental-barrier coating ceramics for resistance against attack by molten calcia-magnesia-aluminosilicate (CMAS) glass: part II, β-$Yb_2Si_2O_7$ and β-$Sc_2Si_2O_7$. J Eur Ceram Soc. 2018;38(11):3914–24. https://doi.org/10.1016/j.jeurceramsoc.2018.03.010
20. Zhao M, Hu X, He J, Li Y, Song W jia. Corrosion behavior and mechanism of ytterbium monosilicate by molten calcium-magnesium-alumino-silicate melts at 1400°C and 1500°C. Ceram Int. 2023;49(14):23756–64. https://doi.org/10.1016/j.ceramint.2023.04.213
21. Klemm H. Silicon nitride for high-temperature applications. J Am Ceram Soc. 2010;93(6):1501–22. https://doi.org/10.1111/j.1551-2916.2010.03839.x
22. Al Nasiri N, Patra N, Horlait D, Jayaseelan DD, Lee WE. Thermal properties of rare-earth monosilicates for EBC on Si-based ceramic composites. J Am Ceram Soc. 2016;99(2):589–96. https://doi.org/10.1111/jace.13982
23. Stolzenburg F, Kenesei P, Almer J, Lee KN, Johnson MT, Faber KT. The influence of calcium-magnesium-aluminosilicate deposits on internal stresses in $Yb_2S_{i2}O_7$ multilayer

environmental barrier coatings. Acta Mater. 2016;105:189–98. https://doi.org/10.1016/j.actamat.2015.12.016

24. Wiesner VL, Harder BJ, Bansal NP. High-temperature interactions of desert sand CMAS glass with yttrium disilicate environmental barrier coating material. Ceram Int. 2018;44(18):22738–43. https://doi.org/10.1016/j.ceramint.2018.09.058
25. Jiang F, Cheng L, Wang Y. Hot corrosion of RE_2SiO_5 with different cation substitution under calcium–magnesium–aluminosilicate attack. Ceram Int. 2017;43(12):9019–23. https://doi.org/10.1016/j.ceramint.2017.04.045
26. Han J, Wang Y, Liu R, Wan F. Theoretical and experimental investigation of Xenotime-type rare earth phosphate $REPO_4$, (RE = Lu, Yb, Er, Y and Sc) for potential environmental barrier coating applications. Sci Rep. 2020;10(1):13681-1. https://doi.org/10.1038/s41598-020-70648-0
27. Du A, Wan C, Qu Z, Pan W. Thermal conductivity of monazite-type $REPO_4$ (RE = La, Ce, Nd, Sm, Eu, Gd). J Am Ceram Soc. 2009;92(11):2687–92. https://doi.org/10.1111/j.1551-2916.2009.03244.x
28. Cho IS, Choi GK, An JS, Kim JR, Hong KS. Sintering, microstructure and microwave dielectric properties of rare earth orthophosphates, $RePO_4$ (Re = La, Ce, Nd, Sm, Tb, Dy, Y, Yb). Mater Res Bull. 2009;44(1):173–8. https://doi.org/10.1016/j.materresbull.2008.03.016
29. Zhao Z, Chen H, Xiang H, Dai FZ, Wang X, Peng Z, et al. $(La_{0.2}Ce_{0.2}Nd_{0.2}Sm_{0.2}Eu_{0.2})PO_4$: a high-entropy rare-earth phosphate monazite ceramic with low thermal conductivity and good compatibility with Al_2O_3. J Mater Sci Technol. 2019;35(12):2892–6. https://doi.org/10.1016/j.jmst.2019.08.012
30. Wang Y, Chen X, Liu W, Cheng L, Zhang L. Exploration of YPO_4 as a potential environmental barrier coating. Ceram Int. 2010;36(2):755–9. https://doi.org/10.1016/j.ceramint.2009.10.014
31. Ridley M, McFarland B, Miller C, Opila E. $YbPO_4$: a novel environmental barrier coating candidate with superior thermochemical stability. Materialia (Oxf). 2022;21:101289–301. https://doi.org/10.1016/j.mtla.2021.101289
32. Padture NP, Gell M, Jordan EH. Thermal barrier coatings for gas-turbine engine applications. Science. 2002;296(5566):280–4. https://doi.org/10.1126/science.1068609
33. Wiesner VL, Scales D, Johnson NS, Harder BJ, Garg A, Bansal NP. Calcium–magnesium aluminosilicate (CMAS) interactions with ytterbium silicate environmental barrier coating material at elevated temperatures. Ceram Int. 2020;46(10):16733–42. https://doi.org/10.1016/j.ceramint.2020.03.249
34. Tian Z, Ren X, Lei Y, Zheng L, Geng W, Zhang J, et al. Corrosion of $RE_2Si_2O_7$ (RE = Y, Yb, and Lu) environmental barrier coating materials by molten calcium-magnesium-alumino-silicate glass at high temperatures. J Eur Ceram Soc. 2019;39(14):4245–54. https://doi.org/10.1016/j.jeurceramsoc.2019.05.036
35. Sun L, Luo Y, Tian Z, Du T, Ren X, Li J, et al. High temperature corrosion of $(Er_{0.25}Tm_{0.25}Yb_{0.25}Lu_{0.25})_2Si_2O_7$ environmental barrier coating material subjected to water vapor and molten calcium–magnesium–aluminosilicate (CMAS). Corros Sci. 2020;175:108881–90. https://doi.org/10.1016/j.corsci.2020.108881
36. Min S, Blumm J, Lindemann A. A new laser flash system for measurement of the thermophysical properties. Thermochim Acta. 2007;455(1–2):46–9. https://doi.org/10.1016/j.tca.2006.11.026
37. Nikiforova GE, Ryumin MA, Gavrichev KS, Gurevich VM. High-temperature thermodynamic properties of $LuPO_4$. Inorg Material. 2012;48(8):841–4. https://doi.org/10.1134/S0020168512080122
38. Liu J, Zhang L, Liu Q, Cheng L, Wang Y. Calcium-magnesium-aluminosilicate corrosion behaviors of rare-earth disilicates at 1400°C. J Eur Ceram Soc. 2013;33(15–16):3419–28. https://doi.org/10.1016/j.jeurceramsoc.2013.05.030
39. Webster RI, Opila EJ. Mixed phase ytterbium silicate environmental-barrier coating materials for improved calcium-magnesium-alumino-silicate resistance. J Mater Res. 2020;35(17):2358–72. https://doi.org/10.1557/jmr.2020.151
40. Xu Y, Hu X, Xu F, Li K. Rare earth silicate environmental barrier coatings: present status and prospective. Ceram Int. 2017;43(8):5847–55. https://doi.org/10.1016/j.ceramint.2017.01.153
41. Xu Y, Li J. Preparation and molten salt corrosion research of composite environmental barrier coatings of $Lu_2Si_2O_7$ and Lu_2SiO_5. Mater Res Innov. 2014;18:S4958–62. https://doi.org/10.1179/1432891714Z.000000000874
42. Feng J, Xiao B, Zhou R, Pan W. Anisotropy in elasticity and thermal conductivity of monazite-type $REPO_4$ (RE = La, Ce, Nd, Sm, Eu and Gd) from first-principles calculations. Acta Mater. 2013;61(19):7364–83. https://doi.org/10.1016/j.actamat.2013.08.043
43. Tian Z, Sun L, Wang J, Wang J. Theoretical prediction and experimental determination of the low lattice thermal conductivity of Lu_2SiO_5. J Eur Ceram Soc. 2015;35(6):1923–32. https://doi.org/10.1016/j.jeurceramsoc.2015.01.001
44. Zhang B, Zhang H, Bai M, Du A, Owusu EB, Lynam A, et al. Thermal properties and calcium-magnesium-alumino-silicate (CMAS) interaction of novel γ-phase ytterbium-doped yttrium disilicate (γ-$Y_{1.5}Yb_{0.5}Si_2O_7$) environmental barrier coating material. Adv Compos Hybrid Mater. 2024;7(2). https://doi.org/10.1007/s42114-024-00879-6
45. Tian Z, Zhang J, Zheng L, Hu W, Ren X, Lei Y, et al. General trend on the phase stability and corrosion resistance of rare earth monosilicates to molten calcium–magnesium–aluminosilicate at 1300°C. Corros Sci. 2019;148:281–92. https://doi.org/10.1016/j.corsci.2018.12.032

SUPPORTING INFORMATION

Additional supporting information can be found online in the Supporting Information section at the end of this article.

How to cite this article: Majee BP, Bryce K, Huang L, Lian J. CMAS corrosion resistance of rare earth phosphates at high temperatures for environmental barrier coatings. J Am Ceram Soc. 2025;108:e20251. https://doi.org/10.1111/jace.20251